ANALYSIS AND PERFORMANCE OF DISPENSED AND SCREEN PRINTED FRONT SIDE CONTACTS AT CELL AND MODULE LEVEL

C. Rodríguez[a], M. Pospischil[b]*, A. Padilla[b], M. Kuchler[b], M. Klawitter[b], T. Geipel[b], M. Padilla[b], T. Fellmeth[b], A. Brand[b], R. Efinger[b], M. Linse[b], H. Gentischer[b], M. König[c], M. Hörteis[c], L. Wende[d], O. Doll[e], F. Clement[b] and D. Biro[b]

[a]Former Fraunhofer ISE, currently at Solar Energy Research Institute of Singapore, National University of Singapore, 7 Engineering Drive 1, 117574, Singapore
[b]Fraunhofer Institute for Solar Energy Systems ISE, Heidenhofstraße 2, 79110 Freiburg, Germany
[c]Heraeus Deutschland GmbH & Co. KG, Heraeusstr. 12-14, D-63450 Hanau, Germany
[d]ASYS Automatisierungssysteme GmbH, Benzstr. 10, 89160 Dornstadt, Germany
[e]Merck KGaA, Postcode Q004/001, Frankfurter Str. 250, D-64293 Darmstadt, Germany
* *Corresponding author. Tel.: +49 (0)761 4588 5268*
E-mail address: maximilian.pospischil@ise.fraunhofer.de

ABSTRACT: In this paper, the potential of applied contact geometries by dispensing, single and double screen printing, are analyzed with respective modeling and simulations at cell and module level. Industrial Cz-Si p-type 156x156 mm² Al-BSF cells are processed to compare the measured values with the estimated ones. A parallel ten nozzle fine line unit is used to print the dispensed fingers while for the screen printing technology, the standard process is applied. An in-depth characterization of the metal contacts by means of laser confocal microscopy, spectrally resolved light beam induced current and micro-light beam induced current (*SR-LBIC* and *µLBIC*, respectively) is conducted and respective values are applied for predicting cell and module results based on these geometrical parameters. Finally, resulting calculations are compared with measured results. The highest efficiency values are obtained for the dispensing technology, up to 19.3% on cell level and 18.3% on module level after light induced degradation (*LID*). The intent of this paper is to obtain the mathematical expressions of cell and module parameters to determine the factors with the highest influence over them. By this, an improvement in the fabrication process can be achieved to enhance their electrical performance and reduce the fabrication costs.
Keywords: Silicon Solar Cell and Module, Metallization, Dispensing, Screen Printing, Mathematical Analysis.

1 INTRODUCTION

Thick film screen printing technology has the highest share of the market with respect to the industrial cell metallization as a result of its contacts reliability and long term stability. In order to improve the electrical performance of the cell and to reduce the material usage, the requirement to print smaller fingers becomes necessary. Nevertheless, the production of thinner fingers leads to an increase of paste spreading [1] and mesh marks [2].

Dispensing technology appears as a process in which thin fingers down to 27 µm [3] with a high homogeneity level and improved finger shape [4] can be produced avoiding the inconvenience of paste spreading and mesh marks. Due to its contactless printing process, pastes may be precisely adapted towards a more beneficial contact geometry [5]. By this, a considerable increase in cell efficiency of up to +0.4%abs. in comparison to single screen printed technology has been previously demonstrated [6]. In order to understand and improve these geometric advantages, a separate analysis of optical and electrical losses was conducted on solar cell and module level.

Nomenclature

A_{cell} (cm^2)	Cell area	r_c (Ω·cm^2)	Area weighted contact resistance of front grid to emitter
A_f (cm^2)	Finger cross-section area		
$A_{o\_BB\_tabs}$ (cm^2)	Optical area covered by the busbars or tabs	r_e (Ω·cm^2)	Area weighted emitter resistance
AL-BSF	Aluminum back surface field	R_{eff} (Ω)	Effective resistance
$A_{o\ f}$ (cm^2)	Optical area covered by the fingers	r_f (Ω·cm^2)	Area weighted finger resistance
AR_o	Optical aspect ratio	$r_{front\ tab}$ (Ω·cm^2)	Area weighted front tab resistance
A_{uc} (cm^2)	Unit cell area	$r_{m\ rs}$ (Ω·cm^2)	Area weighted rear side metal layer resistance
Cz	Czochralski process		
Disp.	Dispensed samples	r_p (Ω·cm^2)	Area weighted shunt resistance
EQE(λ)	External quantum efficiency	r_{rc} (Ω·cm^2)	Area weighted contact resistance of rear side to base
EVA	Ethylene-vinyl acetate		
EW (%)	Relative effective finger width	$r_{rear\ tab}$ (Ω·cm^2)	Area weighted rear tab resistance
FF (%)	Fill factor	r_s (Ω·cm^2)	Area weighted series resistance
I_{uc} (A)	Total current generated in the unit cell	R_{sh} (Ω/sq)	Sheet resistivity
j_L (mA/cm²)	Load current density	r_{sj} (Ω·cm^2)	Area weighted contact resistance of soldering joint
j_{o1} (pA/cm^2)	Dark saturation current density diode 1		
j_{o2} (pA/cm^2)	Dark saturation current density diode 2	*SP(1x)*	Single screen printed samples
j_{ph} (mA/cm²)	Photo-generated current density	*SP(2x)*	Double screen printed samples
j_{sc} (mA/cm²)	Short circuit current density of	*SR-LBIC*	Spectrally resolved light beam

	reference cell		induced current
$j_{sc\ no\ metal}$ (mA/cm²)	Average short circuit current density of non metallized region	T (K)	Cell or module temperature
$j_{sc\ ref}$ (mA/cm²)	Reference short circuit current density	V_L (V)	Load voltage
$j_{sc\ unit\ cell}$ (mA/cm²)	Average short circuit current density of unit cell	V_{oc} (mV)	Open circuit voltage
LID	Light induced degradation process	W_o (µm)	Optical finger width
n_1	Ideality number of diode 1	$W_{unit\ cell}$ (µm)	Unit cell width
n_2	Ideality number of diode 2	ΔA_f (%)	Deviation of the finger cross-section area
P_{e_loss} (W)	Total power losses	λ (nm)	Wavelength
$Pf(\lambda)$ ($m^{-2}\cdot s^{-1}$)	Photon flux	η (%)	Solar cell or module efficiency
r ($\Omega\cdot cm^2$)	Area weighted resistance	Λ_{grid} (%)	Total shading percentage
r_b ($\Omega\cdot cm^2$)	Area weighted base resistance	Λ_{ref} (%)	Total shading percentage of reference cell
r_{BB} ($\Omega\cdot cm^2$)	Area weighted busbar resistance	*µLBIC*	Micro light beam induced current

2 APPROACH

In this study, industrial Cz-Si p-type 156x156 mm² Al-BSF cells with industrial emitters (R_{sh} ~ 90 Ω/sq.) are employed in order to compare the influence of dispensed, single and double screen printed contact fingers on cell results. On each sample, 100 fingers and three single screen printed busbars, whose width is equal to 1.2 mm, are printed, respectively. One-cell modules are fabricated from the previous investigated solar cells that are equipped with standard solar glass, EVA, back sheets and three solder tabs at the top and at the rear side of the cell. The tab width is 1.5 mm and the thickness 0.2 mm. The value of the short circuit current density is estimated considering the influence of the effective finger width which is obtained from three methods based on the *SR-LBIC*, *µLBIC* and on a software tool named "Reflectometer" which was developed for this work, respectively. The area weighted series resistance is then calculated applying the lumped resistance model [7], while the open circuit voltage, fill factor and efficiency are derived from the two diode model [8]. With the previous procedures, a wide analysis of the metallization influence over the cell and module behavior is presented and discussed.

3 RESULTS AND DISCUSSIONS

3.1 Finger analysis

In order to print the dispensed fingers, a parallel ten nozzle (nozzle diameter of 60 µm) fine line unit is applied on a cell with preprinted non-contacting busbars. The screen printed technology is employed to produce single *SP(1x)* and double printed *SP(2x)* fingers, where screens with an opening of 50 µm and 45 µm are applied, respectively. The finger geometry properties are obtained from the Olympus LEXT4000, a commercially available laser confocal microscope, by which a 3D image with a 50x magnification is generated as shown in Figure 1. Two graphs are obtained per sample. The first one assigns a confocal 3D image (Real Image) while the later one shows the extracted height profile (Height Image). It can be appreciated that the dispensed samples present a more homogeneous structure as well as higher slopes with lower paste spread at the edges, in comparison with the screen printed ones.

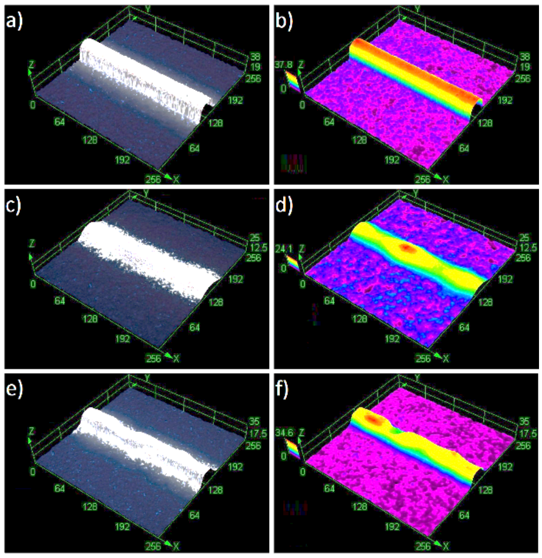

Figure 1: 3D Images of fingers obtained from LEXT microscope.
Dispensed: a) Real Image b) Height Image.
Single Screen Printed: c) Real Image d) Height Image.
Double Screen Printed: c) Real Image d) Height Image.

In the following, a statistical processing of the finger data using an in house developed MATLAB tool took place, as introduced in [4], in which the information provided by the LEXT measurements (finger height, shape, among others) is employed to estimate the optical and electrical finger properties. Different finger parameters are obtained and presented in Figure 2. In average, the optical width (W_o) of the dispensed samples is 41 µm while the one of the single and double screen printed measure 54 µm and 49 µm, respectively. These values show the potential of the first technology because the printed fingers have a lower width in comparison with the diameter of the nozzles (here: 60 µm). Opposite is the case of the latter ones in which the finger width is larger than the screen opening being 50 µm and 45 µm, respectively. An increase of the optical aspect ratio and the homogeneity level enhances the electrical performance of processed solar cells and modules [4]. The relatively high cross-section area, which is on a similar level as the one of the double printed samples, correlates with the diameter of the applied dispensing nozzles in this experiment and was reduced to values below 500 µm² in latest experiments [9].

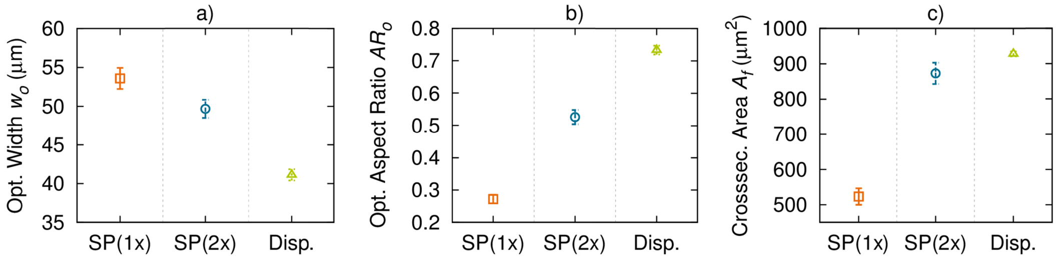

Figure 2: Resulting contact finger geometries of the three investigated groups on industrial Cz156x156 mm² material regarding: (a) optical finger width W_o, (b) optical aspect ratio AR_o and (c) average finger cross-section area A_f.

The optical finger width does not represent the corresponding shading generated by the grid on the solar cell. In order to properly describe these losses, the term Effective Width *EW* is commonly used as it considers the influence of the finger shape [10]. It is the percentage of the area covered by the metallic contacts that is effectively shading the cell. To obtain the *EW*, a method performed with the *SR-LBIC* is proposed in [11] and performed in [12], the same procedure is also applied with the *µLBIC*. The working principle consists in defining a unit cell in the solar cell (which contains one finger) with width W_{unit_cell} and measure the local j_{sc} of the whole region of the unit cell and of a region that is non metallized, with average values of $j_{sc\_unit\_cell}$ and $j_{sc\_no\_metal}$, respectively. The *EW* can then be calculated as shown in Eq.(1).

$$EW = \left(1 - \frac{j_{sc\_unit\_cell}}{j_{sc\_no\_metal}}\right) \cdot \frac{W_{unit\_cell}}{w_o} \cdot 100\% \qquad (1)$$

It was the intention of this study to compare the results obtained from the *LBIC* and *µLBIC* analysis, as the setup of the *LBIC* is much simpler and samples do not have to be specially prepared. However, the resolution of the *µLBIC* is significantly higher than the one of the employed *LBIC* (3.13 µm vs 50 µm). Nevertheless, this difference should be irrelevant for the proposed method, due to the high number of applied measuring points.

A program designed in MATLAB named "Reflectometer" is also employed to estimate the *EW* applying the ray tracing analysis. It considers the height information of the sample obtained from the LEXT, the light absorption coefficient in silver, percentage of direct and indirect reflection, refractive index of the solar glass and air as well as the application of Snell's law and Fresnel equations, among others. Due to equipment limitation, the *LBIC* and *µLBIC* measurements were not able to be performed at the same wavelength value but at 780 nm and 826 nm, respectively, which are close values, so that a similar behavior is expected. The results are shown in Figure 3.

As expected, the *EW* at module level is lower than the one at cell level (due to the internal reflection within the module) which means that the finger influence of shading losses decreases if the cell is incorporated into a module. The *EW* obtained from the *LBIC* and *µLBIC* analysis are similar; the simulated results obtained from the Reflectometer are also comparable to the previous methods with respect to the dispensing technology. Nevertheless, larger differences between the calculated and simulated results are presented for the case of the screen printed samples, this is because the exact local shape of these fingers has not yet been considered due to their higher amount of paste spread, which makes it more difficult to recognize the finger edge at the simulation level.

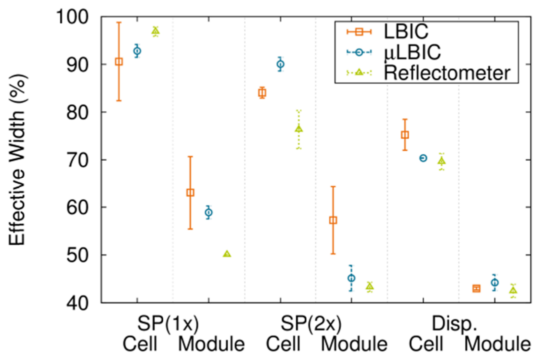

Figure 3: Effective finger width calculation at the cell and module level based on the LBIC (at 780 nm), µLBIC (at 826 nm) and Reflectometer (at 780 nm) methods.

3.2 Electrical analysis

<u>Short circuit current density (j_{sc}) approximation</u>

The j_{sc} can be estimated from the *EW* values in order to reflect the properties of the metal fingers, despite later processing fluctuations. The previous method based on the SR-LBIC is considered to estimate j_{sc}. In order to take into account the solar spectrum influence, the *EW* value is obtained for six different wavelengths (405 nm, 532 nm, 658 nm, 780 nm, 940 nm and 1064 nm) and then is weighted with respect to the photon flux, as shown in Eq.(2) The average results are presented in Table 1.

$$Weighted\ EW = \frac{\sum_\lambda (EW(\lambda) \cdot EQE(\lambda) \cdot Pf(\lambda))}{\sum_\lambda (EQE(\lambda) \cdot Pf(\lambda))} \qquad (2)$$

Where *EQE(λ)* is the measured external quantum efficiency of the cell or module and *Pf(λ)* the photon flux for a wavelength λ.

The principle to estimate j_{sc} consists in the indirect relation between this value and the amount of shading regions on the cell. The total percentage of shading A_{grid} on the cell (with area A_{cell}) due to the optical area covered by the fingers A_{o_f}, busbars and tabs $A_{o\_BB\_tabs}$ (busbars are considered at the cell level while tabs at the module level) is obtained from Eq.(3), their average values are given in Table 1.

$$A_{grid} = \frac{(A_{o\_f} \cdot Weighted\ EW) + A_{o\_BB\_tabs}}{A_{cell}} \cdot 100\% \qquad (3)$$

Subsequently, they are compared with a reference cell with a known short circuit current density j_{sc_ref} and shading percentage Λ_{ref}, as shown in Eq.(4)

$$j_{sc} = \frac{1-\Lambda_{grid}}{1-\Lambda_{ref}} \cdot j_{sc\_ref} \quad (4)$$

Table 1: Average values of the weighted effective widths, optical area covered by the fingers, busbars and tabs and shading percentage at the cell and module level.

	SP(1x)		SP(2x)		Disp.	
	cell	**mod**	**cell**	**mod**	**cell**	**mod**
Weighted EW (%)	95	72	87	60	72	46
A_{o_f} **(cm²)**	8.2	7.9	7.5	7.2	6.2	6.0
$A_{o\_BB\_tabs}$ **(cm²)**	5.3	14	5.3	14	5.3	14
Λ_{grid} **(%)**	5.4	8.1	4.8	7.6	4.0	6.9

The estimated results of j_{sc} as well as the measured ones are presented in Figure 4. A small deviation between estimated and measured values supports the assumption previously considered of the relation between j_{sc} and the amount of shading losses. As expected, due to a lower optical and effective width, the j_{sc} for the dispensing technology is the highest followed by the *SP(2x)* and *SP(1x)*. Despite the lower *EW* and increased absorption of light on the anti-reflection coating as a result of the internal reflection, the average j_{sc} produced at module level tends to be lower than the one at the cell level. The main reasons for that are due to the external reflection at the glass surface and absorption losses in the glass and EVA layers.

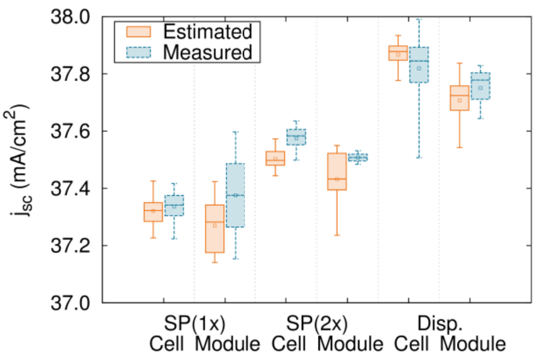

Figure 4: Estimated and measured short circuit current density at the cell and module level for the different finger technologies.

<u>Area weighted series resistance (r_s) approximation</u>

After considering optical losses in the previous part, this section closely investigates ohmic losses contributing to the series resistance of the cell or module [8]. To obtain the individual contributions of the series resistance, as shown in Figure 5, the lumped series resistance model [7] is applied. This model relates the different series resistance contributions to their respective unit cell area (this value can then be the applied to the whole cell due to the unit cell periodicity). The total series resistance r_s corresponds to the sum of all weighted contributions.

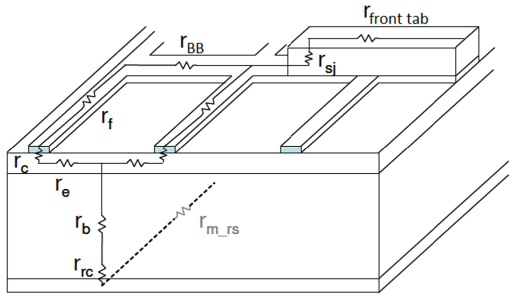

Figure 5: Series resistance components (adapted from [8]).

The equations that represent each resistance contribution have been previously developed in [8]. In this paper, however, improved approximations for the weighted base and busbar resistance contributions are employed. These equations are located in the Appendix section.

The contributions of the series resistance are represented in pie charts, as shown in Figure 6.

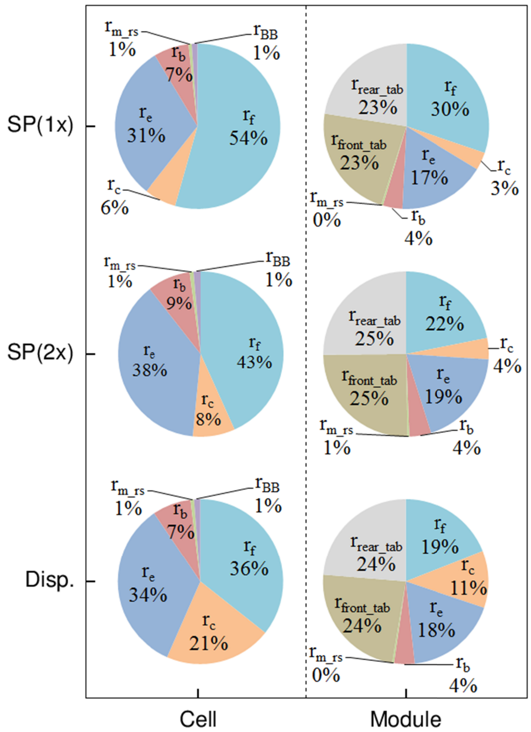

Figure 6: Area weighted series resistance contributions at cell and module level for the analyzed finger technologies.

The graphs in Figure 6 reveal that for the dispensed cells, the finger resistance (r_f) has a lower contribution in comparison to the screen printed cells. This result is due to the larger metallized area on the cell surface and consequently lower ohmic losses. Contrarily, the dispensing technology imposes a higher contact resistance of the front grid to the emitter due to the applied dispensing paste in this experiment which has not yet been a commercially available screen printing paste. At module level, the influence of the tabs represents about 50% of the whole series resistance. Figure 7 presents the estimated and measured (obtained from the illuminated and dark IV curve characteristics, defined as

"R_{s_light}" in [13]) values which are similar at cell level but have a higher deviation at module level. This could be due to the impact of the cell gaps and cross connectors that were not considered when performing the estimation. Relatively close values were obtained for all technologies. This demonstrates that the dispensing technology does not cause higher ohmic losses at cell and module level. The module resistance is almost twice as high as the one at cell level, mostly because of the soldered tabs contribution.

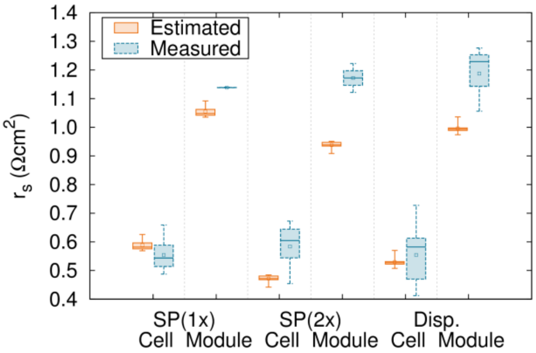

Figure 7: Estimated and measured values of the area weighted series resistance at the cell and module level for the different metallization technologies.

<u>Two diode model approximation</u>

Finally, the two diode model, which is represented by Eq.(5), is proposed to approximate the value of the fill factor (*FF*), open circuit voltage (V_{oc}) and efficiency (η) considering the previously estimated values for r_s and j_{sc}.

$$j_L = j_{ph} - j_{o1} \cdot \left(exp\left[\frac{e \cdot (V_L + j_L \cdot r_s)}{n_1 \cdot K_B \cdot T}\right] - 1 \right) - j_{o2} \cdot \left(exp\left[\frac{e \cdot (V_L + j_L \cdot r_s)}{n_2 \cdot K_B \cdot T}\right] - 1 \right) - \frac{V_L + j_L \cdot r_s}{r_P} \quad (5)$$

The following considerations are applied:

- j_{ph} (mA/cm^2): Photo-generated current density, assumed to be equal to the estimated j_{sc}.
- j_{o1} (pA/cm^2): Dark saturation current density of diode one. It is obtained by fitting the measured dark IV curve on the two diode model based on the orthogonal distance regression method [14].
- j_{o2} (pA/cm^2): Dark saturation current density of diode two. It is obtained by fitting the measured dark IV curve on the two diode model based on the orthogonal distance regression method [14].
- r_p (Ω·cm^2): Area weighted shunt resistance, obtained from the relation of the voltage with respect to the current density of the approximated slope of the dark IV curve within a range of -50 mV to 50 mV.
- n_1: Ideality number of diode one. Assuming the ideal case ($n_1 = 1$).
- n_2: Ideality number of diode two. Assuming the ideal case ($n_2 = 2$).
- T (K): Cell or module temperature. Assuming that the cell or module is at an ambient temperature of 298 K.
- K_B (*e*V/K): Boltzmann constant.
- e (C): Electron charge.
- V_L (V): Load voltage.
- j_L (mA/cm^2): Load current density.

The measured r_p is higher than 10.0 kΩ·cm^2. Due to this high value, it can then be disregarded for the following calculations [7].

The efficiency results are shown in Figure 8.

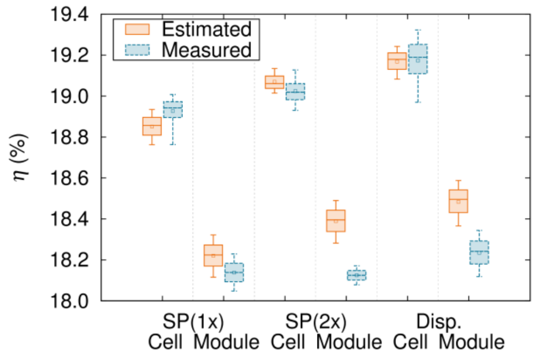

Figure 8: Estimated and measured efficiency at the cell and module level for the different metallization technologies.

The estimated efficiency of the dispensed contacts is higher than the one of the *SP(1x)* and *SP(2x)* (in average, 19.2% vs. 18.9% and 19.1% at the cell level and 18.5% vs. 18.2% and 18.4% at the module level, respectively). This result is because of the high advantage that the former has due to its higher j_{sc}. At cell level, the estimated and measured results are similar, the measured values at module level are lower than the predicted ones due to the lower assumed series resistance of the latter. The drop in efficiency from cell to module level is mostly due to the effects from *LID* [15], an increase of the series resistance, the reflection loss of light at the glass surface and the absorption losses within the glass and EVA layers [16].

4 CONCLUSIONS AND OUTLOOK

In this study, a comparison between simulated and experimental data of cell and module parameters based on dispensed and screen printed fingers was conducted. The finger geometry analysis reveals that the dispensing technology generates fingers with smaller optical widths in comparison to single and double screen printed samples (41.2 µm vs. 53.8 µm and 49.4 µm). The previous analysis, together with a smaller weighted effective width (72.4% vs. 95.5% and 87.2% at the cell level and 45.9% vs. 72.0% and 60.4% at the module level) due to an improved finger shape, leads to a significant increase of the short circuit current density [4]. The measured effective width results obtained from the *LBIC* and the *µLBIC* are quite similar, which means that the former is good enough in order to perform a reliable analysis; without the necessity to destroy the measurement sample during preparation, thus saving costs and time. The average estimated efficiencies show a deviation of less than 0.1% and 0.3% in comparison with the measured ones at the cell and module level, respectively; this proves the reliability of the conducted calculations. The advantages presented at the dispensing fingers are the reasons why both analysis reveal a higher performance at the cell and module level (both times approx. +0.3% abs. in average).

In the meantime, dispensing technology improvements on similar material but applying pastes designed for screen printing and using nozzle diameters of only 40 µm during continuous printing, led to both, further increasing cell efficiencies (up to 19.7%) at decreasing finger cross-section A_f (down to 500 µm²) [9]. Where the latter correlates with a substantially reduced wet paste laydown of only 70 mg per wafer for the dispensed contact fingers + 20mg for dual printed busbars. Based on this new status, four cell modules of these high efficient Al-BSF samples are currently characterized at Fraunhofer ISE CalLab and will be presented at the conference.

5 ACKNOWLEDGEMENTS

The authors would like to thank all co-workers at the Photovoltaic Technology Evaluation Center (PV-TEC) and the module department. This work was supported by the German Federal Ministry for Economic Affairs and Energy within the research project "GECKO" under contract number 0325404.

6 APPENDIX

6.1 Area weighted series resistance (r_s) calculation

The lumped series resistance model applied to obtain r_s works as follows:

1. Select the resistance contribution of interest, as shown in Figure 5.
2. Define its unit cell region, as shown in Figure 9.
3. Calculate the effective resistance R_{eff}, as defined in Eq.(6). P_{e_loss} and I_{uc} represent the total power losses of the chosen resistance from step one and the total current generated in the unit cell, respectively.

$$R_{eff} = \frac{P_{e\_loss}}{I_{uc}^{2}} \tag{6}$$

4. The area weighted resistance r is calculated from Eq.(7). A_{uc} represents the unit cell area.

$$r = R_{eff} \cdot A_{uc} \tag{7}$$

5. The previous steps are repeated to calculate all the resistance contributions. The addition of all is equal to r_s.

The unit cells required to apply the previous steps for all the resistance contributions are shown in Figure 9.

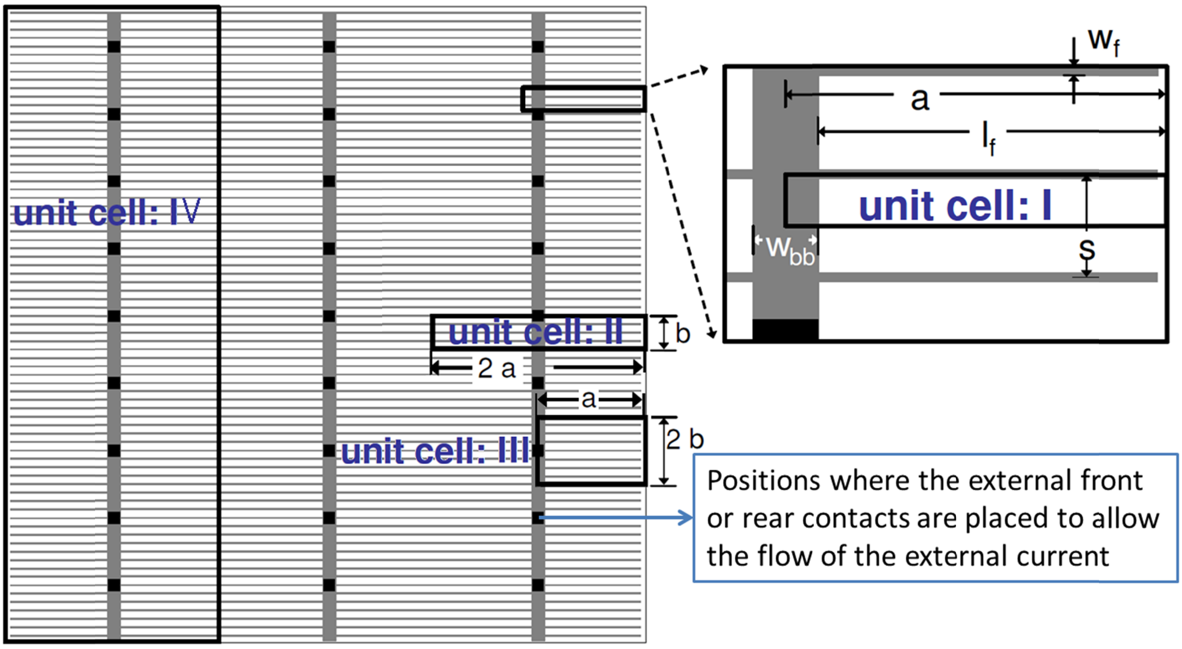

Figure 9: Defined unit cells in a solar cell with three busbars (slightly modified from [8]).

The final equations are presented in Table 2:

Table 2: Unit cell area, resistance from that unit cell and area weighted resistance contributions to the series resistance, as defined in [8].

Resistance	Unit cell (cm^2)	R_{eff}: Resistance of the unit cell (Ω)	r: Area weighted resistance (Ω·cm^2)
Rear side metal layer	III: $a\cdot 2\cdot b_{rear}$	$\frac{\rho_{m\_rs}\cdot l_f}{6\cdot b_{rear}\cdot h_{m\_rs}}$	$\frac{\rho_{m\_rs}\cdot l_f\cdot a}{3\cdot h_{m\_rs}}$
Base	A_{cell}	$\frac{\rho_b\cdot Th_{cell}}{A_{cell}}$	$\rho_b\cdot Th_{cell}$
Emitter	I: $a\cdot\frac{s}{2}$	$\frac{R_{sh}\cdot(s-w_f)}{6\cdot l_f}$	$\frac{R_{sh}\cdot(s-w_f)\cdot a\cdot s}{12\cdot l_f}$
Contact of finger to emitter	I: $a\cdot\frac{s}{2}$	$\frac{\sqrt{R_{sh}\cdot\rho_c}}{l_f}\cdot coth\left(\frac{w_f}{2}\cdot\sqrt{\frac{R_{sh}}{\rho_c}}\right)$	$\frac{a\cdot s\cdot\sqrt{R_{sh}\cdot\rho_c}}{2\cdot l_f}\cdot coth\left(\frac{w_f}{2}\cdot\sqrt{\frac{R_{sh}}{\rho_c}}\right)$
Finger	I: $a\cdot\frac{s}{2}$	$\frac{2\cdot\rho_f\cdot l_f}{3\cdot h_f\cdot w_f}$	$\frac{\rho_f\cdot l_f\cdot a\cdot s}{3\cdot h_f\cdot w_f}$
Busbar	II: $2\cdot a\cdot b_{front}$	$\frac{\rho_{BB}\cdot b_{front}}{3\cdot h_{BB}\cdot w_{BB}}$	$\frac{2\cdot a\cdot\rho_{BB}\cdot b_{front}^2}{3\cdot h_{BB}\cdot w_{BB}}$
Front Tab	IV: $2\cdot a\cdot l_{cell}$	$\frac{\rho_{front\_tab}\cdot l_{cell}}{6\cdot h_{front\_tab}\cdot w_{tab}}\cdot\frac{2\cdot n_f^2+1}{n_f^2}$	$\frac{a\cdot\rho_{front\_tab}\cdot l_{cell}^2}{3\cdot h_{front\_tab}\cdot w_{front\_tab}}\cdot\frac{2\cdot n_f^2+1}{n_f^2}$
Rear Tab	IV: $2\cdot a\cdot l_{cell}$	$\frac{\rho_{rear\_tab}\cdot l_{cell}}{6\cdot h_{rear\_tab}\cdot w_{tab}}\cdot\frac{2\cdot n_{Ag\_pads}^2+1}{n_{Ag\_pads}^2}$	$\frac{a\cdot\rho_{rear\_tab}\cdot l_{cell}^2}{3\cdot h_{rear\_tab}\cdot w_{rear\_tab}}\cdot\frac{2\cdot n_{Ag\_pads}^2+1}{n_{Ag\_pads}^2}$

The variables employed in the previous table are described in Table 3:

Table 3: List of constants and variables required to obtain the resistance contributions.

Symbol	Description	Unit	Symbol	Description	Unit
a	Length of unit cell I and III	m	n_{Ag_pads}	Number of silver pads at rear side per column	-
A_{cell}	Cell area	m^2	n_f	Number of fingers	-
$A_{cell\_non\_met}$	Non metallized	m^2	R_{sh}	Emitter sheet resistance	Ω/□
	cell area		s	Finger separation	m
b_{front}	Length of unit cell II	m	Th_{cell}	Cell thickness	m
	considering the front		w_{BB}	Busbar width	m
	external connectors		w_f	Finger width	m
b_{rear}	Length of unit cell II	m	w_{front_tab}	Front tab width	m
	considering the rear		w_{rear_tab}	Rear tab width	m
	external connectors /		ρ_b	Base line resistivity	Ω·m
	silver pads		ρ_{BB}	Busbar line resistivity	Ω·m
h_{BB}	Busbar height	m	ρ_c	Front contact resistivity	Ω·m^2
h_f	Finger height	m		(finger to emitter)	
h_{m_rs}	Metar rear side	m	ρ_f	Finger line resistivity	Ω·m
	height		ρ_{front_tab}	Front tab line resistivity	Ω·m
h_{front_tab}	Front tab height	m	ρ_{m_rs}	Metal rear side line	Ω·m
h_{rear_tab}	Rear tab height	m		resistivity	
l_{cell}	Cell length	m	ρ_{rear_tab}	Rear tab line resistivity	Ω·m
l_f	Finger length in	m			
	unit cell I				

In this paper, as indicated in section "3.2 Electrical analysis", improved approximations to obtain the resistance contributions of the base and busbar are applied and presented in Table 4:

Table 4: Improved approximation to obtain the resistance and area weighted resistance contributions of the base and busbar.

Resistance	Unit cell (cm^2)	R_{eff}: Resistance of the unit cell (Ω)	r: Area weighted resistance (Ω·cm^2)
Base	A_{cell}	$\frac{\rho_b \cdot Th_{cell}}{A_{cell\_non\_met}}$	$\rho_b \cdot Th_{cell} \cdot \frac{A_{cell}}{A_{cell\_non\_met}}$
Busbar	II: $2 \cdot a \cdot b_{front}$	$\frac{\rho_{BB} \cdot (2 \cdot b_{front}{}^2 + s^2)}{6 \cdot b_{front} \cdot h_{BB} \cdot w_{BB}}$	$\frac{a \cdot \rho_{BB} \cdot (2 \cdot b_{front}{}^2 + s^2)}{3 \cdot h_{BB} \cdot w_{BB}}$

The procedure from [8], to calculate the base contribution, assumes that the photons are absorbed through the whole cell area A_{cell}, while the improved method considers that this occurs only at the effective non-metallized regions $A_{cell\_non\_met}$ in which the *EW* is also taken into account.

The method to obtain the busbar contribution, as indicated in [8], assumes that the amount of current flowing through the busbar increases linearly along its length. The improved method considers that the current increases by a constant step value at the locations where the fingers intersect with the busbar. This last one is a better approximation as most of the current is first transported through the fingers in order to reach the busbar.

7 REFERENCES

[1] M. Aoki, et al., "30µm fine-line printing for solar cells", in Photovoltaic Specialists Conference (PVSC), pp. 2162-2166, 2013.

[2] L. Jiang, et al., "An improved mathematical modeling to simulate metallization screen pattern trend for silicon solar cell", in Photovoltaic Specialists Conference (PVSC), pp. 2641-2645, 2013.

[3] M. Pospischil, et al., "Process development for a high-throughput fine line metallization approach based on dispensing technology", Energy Procedia, vol. 43, pp. 111-116, 2013.

[4] M. Pospischil, et al., "Optimizing fine line dispensed contact grids", Energy Procedia, vol. 55, pp. 693-701, 2014.

[5] M. Pospischil, et al., "Paste Rheology Correlating With Dispensed Finger Geometry", IEEE Journal of Photovoltaics, vol. 4, pp. 498-503, 2014.

[6] M. Pospischil, et al., "Ultrafine Front Side Metallization on Silicon Solar Cells by Industrial Dispensing Technology", in 29th EU-PVSEC, Amsterdam, The Netherlands, 2014.

[7] A. Goetzberger, et al., “Crystalline silicon solar cells”, Chichester, UK: John Wiley & Sons Ltd., 1998.

[8] A. Mette, "New Concepts for Front Side Metallization of Industrial Silicon Solar Cells", Fraunhofer-Institut für Solare Energiesysteme, Albert-Ludwigs-Universität Freiburg im Breisgau, Freiburg im Breisgau, Germany, 2007.

[9] M. Pospischil, et al., "Progress on industrial solar cell front side metallization by parallel dispensing technology", in 31st EU-PVSEC, Hamburg, Germany, 2015.

[10] R. Woehl, et al., "Analysis of the optical properties of screen-printed and aerosol-printed and plated fingers of silicon solar cells ", Advances in OptoElectronics, vol. 2008, 2008.

[11] M. Beutel, et al., "Fine line metallization by coextrusion technology for next generation solar cells", Solar Energy Materials and Solar Cells, vol. 131, pp. 64-71, 2014.

[12] M. Pospischil, et al., "Dispensing Technology on the Route to an Industrial Metallization Process", Energy Procedia, vol. 67, pp. 138-146, 2015.

[13] A. Aberle, et al., "A new method for accurate measurements of the lumped series resistance of solar cells", in Photovoltaic Specialists Conference, 1993, Conference Record of the Twenty Third IEEE, pp. 133-139, 1993.

[14] A. Burgers, et al., "Improved treatment of the strongly varying slope in fitting solar cell IV curves", in Photovoltaic Specialists Conference, 1996., Conference Record of the Twenty Fifth IEEE, 1996, pp. 569-572, 1996.

[15] A. Das, et al., "The impact of cell design on light induced degradation in p-type silicon solar cells", in Photovoltaic Specialists Conference (PVSC), 2011 37th IEEE, pp. 158-164, 2011.

[16] I. Haedrich, et al., "Unified methodology for determining CTM ratios: Systematic prediction of module power", Solar Energy Materials and Solar Cells, vol. 131, pp. 14-23, 2014.